Bret H. Goodpaster,[1] Alessandra Bertoldo,[2] Jason M. Ng,[1] Koichiro Azuma,[1] R. Richard Pencek,[1] Carol Kelley,[1] Julie C. Price,[3] Claudio Cobelli,[2] and David E. Kelley[1]

Interactions Among Glucose Delivery, Transport, and Phosphorylation That Underlie Skeletal Muscle Insulin Resistance in Obesity and Type 2 Diabetes: Studies With Dynamic PET Imaging

Dynamic positron emission tomography (PET) imaging was performed using sequential tracer injections ([^{15}O]H_2O, [^{11}C]3-O-methylglucose [3-OMG], and [^{18}F]fluorodeoxyglucose [FDG]) to quantify, respectively, skeletal muscle tissue perfusion (glucose delivery), kinetics of bidirectional glucose transport, and glucose phosphorylation to interrogate the individual contribution and interaction among these steps in muscle insulin resistance (IR) in type 2 diabetes (T2D). PET imaging was performed in normal weight nondiabetic subjects (NW) (n = 5), obese nondiabetic subjects (OB) (n = 6), and obese subjects with T2D (n = 7) during fasting conditions and separately during a 6-h euglycemic insulin infusion at 40 mU·m^{-2}·min^{-1}. Tissue tracer activities were derived specifically within the soleus muscle with PET images and magnetic resonance imaging. During fasting, NW, OB, and T2D subjects had similar [^{11}C]3-OMG and [^{18}F]FDG uptake despite group differences for tissue perfusion. During insulin-stimulated conditions, IR was clearly evident in T2D (P < 0.01), and [^{18}F]FDG uptake by muscle was inversely correlated with systemic IR (P < 0.001). The increase in insulin-stimulated glucose transport was less (P < 0.01) in T2D (twofold) than in NW (sevenfold) or OB (sixfold) subjects. The fractional phosphorylation of [^{18}F]FDG during insulin infusion was also significantly lower in T2D (P < 0.01). Dynamic triple-tracer PET imaging indicates that skeletal muscle IR in T2D involves a severe impairment of glucose transport and additional impairment in the efficiency of glucose phosphorylation.

Diabetes 2014;63:1058–1068 | DOI: 10.2337/db13-1249

The rate of glucose uptake into skeletal muscle during insulin-stimulated conditions is a strong determinant of systemic insulin sensitivity (and insulin resistance [IR]). Much of the control of glucose uptake into skeletal muscle is located at the steps of glucose delivery, transport, and phosphorylation (1–4). Among these loci of

[1]Department of Medicine, University of Pittsburgh, Pittsburgh, PA
[2]Department of Information Engineering, University of Padova, Padova, Italy
[3]Department of Radiology, University of Pittsburgh, Pittsburgh, PA
Corresponding author: Bret H. Goodpaster, bret.goodpaster@flhosp.org.
Received 14 August 2013 and accepted 6 November 2013.

This article contains Supplementary Data online at http://diabetes.diabetesjournals.org/lookup/suppl/doi:10.2337/db13-1249/-/DC1.

© 2014 by the American Diabetes Association. See http://creativecommons.org/licenses/by-nc-nd/3.0/ for details.

PATHOPHYSIOLOGY

metabolic control, stimulation of glucose transport mediated by translocation of GLUT4 in response to insulin is crucial (5–7). The small accumulation of glucose within insulin-stimulated muscle has provided supporting evidence that defects in glucose transport are primarily responsible for skeletal muscle IR (4,8–10). The small intracellular accumulation of glucose, however, could also be consistent with defects in glucose delivery (11). Studies using positron emission tomography (PET) have revealed that most of the insulin-stimulated control of glucose uptake in lean, nondiabetic human skeletal muscle is nearly equally distributed between glucose delivery and transport (12). The relative contribution of glucose delivery and transport within skeletal muscle in obesity and type 2 diabetes (T2D) remains uncertain.

Defects in glucose phosphorylation in response to insulin can also potentially contribute to IR. Animal models suggest that glucose phosphorylation capacity may limit glucose uptake when the capacity for glucose transport is high (13,14), although genetic manipulation of the glucose phosphorylation capacity by hexokinase overexpression appears to be less influential during insulin stimulation (1,14). In dynamic PET imaging studies quantifying rates of glucose delivery, transport, and phosphorylation using [^{15}O]H_2O, [^{11}C]3-O-methylglucose (3-OMG), and [^{18}F]fluorodeoxyglucose (FDG), respectively, Bertoldo et al. (12) reported that glucose phosphorylation represented an additional locus of control governing insulin-stimulated rates of glucose uptake in skeletal muscle of lean, healthy subjects. It is not clear, however, the degree to which skeletal muscle IR in obesity or T2D can be attributed to the control of glucose transport and phosphorylation.

The purpose of the current clinical investigation was to use dynamic in vivo PET imaging to dissect out potential loci of skeletal muscle IR in obesity and T2D. We used the triple-tracer method developed by Bertoldo et al. (12) to quantify rates of glucose delivery, transport, and phosphorylation during fasting (basal) and insulin-stimulated conditions. The present study provides novel in vivo quantitative information regarding the contribution and interaction of these proximal steps to skeletal muscle IR.

RESEARCH DESIGN AND METHODS

Research Volunteers

Informed, written consent was obtained from all participants, and the protocol was approved by the University of Pittsburgh Institutional Review Board. Three groups of research volunteers were recruited by advertisement: normal weight, nondiabetic (NW); overweight or obese nondiabetic (OB); and patients with T2D. NW is considered the control group in this study. The clinical characteristics are shown in Table 1; groups were well matched for age and sex distribution, and OB and T2D groups were closely matched for BMI. Blood lipoprotein levels were similar among groups, although plasma triglycerides tended to be higher in T2D. All participants had a medical examination to verify good health. Participants with T2D were treated with lifestyle measures alone or with metformin, which was withheld 3 days before the metabolic studies.

Table 1—Clinical characteristics

	NW	OB	T2D
Sex (female:male)	3:2	3:3	3:4
Age (years)	48 ± 2	46 ± 2	48 ± 2
Weight (kg)	71 ± 6†	93 ± 6	98 ± 5
Height (cm)	173 ± 4	173 ± 4	175 ± 3
BMI (kg/m^2)	23.7 ± 1.2†	31.0 ± 1.1	31.7 ± 1.2
BSA (m^2)	1.8 ± 0.1	2.1 ± 0.1	2.1 ± 0.1
HbA_{1c} (%)	5.4 ± 0.1	5.4 ± 0.1	7.3 ± 0.6*
HbA_{1c} (mmol/mol)	36 ± 1	36 ± 1	56 ± 1
Total cholesterol (mg/dL)	191 ± 13	195 ± 16	190 ± 10
HDL (mg/dL)	65 ± 6	48 ± 7	48 ± 8
LDL (mg/dL)	112 ± 11	120 ± 14	116 ± 5
VLDL (mg/dL)	14 ± 3	27 ± 5	26 ± 4
Triglycerides (mg/dL)	90 ± 17	167 ± 30	160 ± 25
Fasting glucose (mg/dL)	84 ± 5	86 ± 2	131 ± 16

Data are mean ± SEM unless otherwise indicated. BSA, body surface area. †$P < 0.05$ vs. OB and T2D. *$P < 0.05$ vs. NW and OB.

Metabolic Studies

All participants underwent two sessions of triple-tracer PET imaging: one during fasting conditions (basal) and another, in random order, during steady-state insulin-stimulated conditions (insulin), as described below. On the evening before a study, research volunteers were admitted to the University of Pittsburgh Clinical Translational Research Center and fasted overnight. In the morning, catheters were placed in an antecubital vein for infusions and in a radial artery for blood sampling. During basal studies, volunteers did not receive insulin or dextrose infusions. During insulin studies, insulin was infused for 6 h at 40 mU $\cdot$ m^{-2} $\cdot$ min^{-1}, arterial glucose was measured at 5-min intervals, and euglycemia was maintained by an adjustable infusion of 20% dextrose. Arterial glucose was measured with a YSI glucose analyzer (Yellow Springs, OH). Plasma insulin was measured by radioimmunoassay, and plasma fatty acids were measured by colorimetric enzymatic assay (Wako NEFA C test kit; Wako Chemicals, Richmond, VA).

PET and Magnetic Resonance Imaging

PET and magnetic resonance imaging (MRI) was performed at the University of Pittsburgh PET Center and the Magnetic Resonance Research Center using procedures previously described (12). Briefly, a Siemens/CTI ECAT HR+ PET scanner was used in the three-

dimensional imaging mode (63 parallel planes; axial field-of-view = 15.2 cm, slice width = 2.4 mm), and the final reconstructed PET image resolution was ~6 mm. Participants were positioned in the PET scanner with the midcalf area in the center of the field.

[^{15}O]H_2O Imaging

[^{15}O]H_2O was given as an ~30-mCi bolus, and arterial blood sampling was obtained with a Siemens liquid activity monitor. PET scanning began with the injection and lasted 3 min (18 frames of 10 s duration each). PET data were corrected for radioactive decay and scatter (15). During insulin studies, the insulin infusion was given for at least 2 h before PET imaging.

[^{11}C]3-OMG Imaging

[^{11}C]3-OMG was administered as a slow bolus of ~5 mCi ~30 min after completing PET imaging of [^{15}O]H_2O, and dynamic PET scan was started (90 min; 36 frames; 8 of 15 s duration, 8 of 30 s duration, 4 of 1 min duration, and 16 of 5 min duration). Arterial [^{11}C]3-OMG was measured in 0.5-mL samples obtained manually (10 samples every 6 s, 8 samples every 15 s, 7 samples every 1 min, 10 samples every 5 min, and 3 samples every 10 min). Blood samples were immediately centrifuged, and 200 μL of plasma was removed for immediate [^{11}C] counting with a COBRA Auto-Gamma model 5003 gamma counter (Packard Instruments, Meriden, CT).

[^{18}F]FDG Imaging

Two hours after injection of [^{11}C]3-OMG, ~6 mCi [^{18}F]FDG was given as a slow intravenous bolus, and dynamic PET scanning was started (90 min; 28 frames; 8 of 30 s duration, 8 of 60 s duration, 8 of 4 min duration, and 4 of 8 min duration). Arterial blood draws were made for determining [^{18}F]FDG activity (10 × 6 s, 8 × 15 s, 7 × 1 min, 10 × 5 min, and 3 × 10 min). Blood was immediately centrifuged, and 100 μL of plasma was used for [^{18}F] counting (>350 KeV).

MRI of Skeletal Muscle

A T1-weighted MRI of the midcalf was obtained on the same day as the PET imaging session and consisted of a series of T1-weighted images (acquisition parameters: axial plane, repetition time = 31 ms, echo time = 15 ms, flip angle = 10°, field of view = 40 × 20 cm, matrix size = 256 × 192 × 120, partition thickness = 1.5 mm, contiguous partitions, 1 average, total acquisition time = 12.75 min) acquired for high-resolution anatomy. The MRIs were aligned to PET images by a previously described method (16,17). Briefly, summation PET images were created from the frames of the initial 15 min of the scanning period and coregistered with MRI so that precise anatomical alignment was achieved.

Measuring Tissue Activity in PET Images

A region of interest (ROI) was placed over soleus muscles on the summation PET images and MRIs, and these ROIs were applied to each frame (18 for [^{15}O]H_2O, 36 for [^{11}C]3-OMG, and 28 for [^{18}F]FDG) across 58 of the 68 planes of each leg, omitting the proximal and distal 5 planes to reduce the influence of scatter. Tracer activity within an ROI was converted to radioactivity concentration (μCi/mL) using an empiric phantom-based calibration factor (μCi/mL/PET counts per pixel).

Compartmental Modeling

[^{15}O]H_2O

The model of Kety (18) was used to estimate tissue perfusion of skeletal muscle.

[^{11}C]3-OMG

Compartmental modeling of [^{11}C]3-OMG kinetics was performed, as previously described in detail (19,20). Briefly, this model has three compartments (plasma and two tissue pools) with four rate constants as shown in Fig. 1*A*. The rate constants k_1 (mL/mL/min) and k_2 (min^{-1}) describe a reversible exchange between plasma and the first tissue compartment and are ascribed physiologically to an exchange of [^{11}C]3-OMG between the capillary and the muscle interstitial space. The rate constants k_3 (min^{-1}) and k_4 (min^{-1}) describe a reversible exchange between the first and second tissue compartments and are ascribed physiologically to bidirectional transmembrane glucose transport. From these rate constants, an overall partition coefficient V_d for uptake of [^{11}C]3-OMG from plasma to tissue can be calculated and is divisible into a partition coefficient for the first compartment, muscle interstitial space V_{ic}, and a partition coefficient for the tissue compartment V_{ec}, as shown in Eq. 1:

$$V_d = V_{ec} + V_{ic} = \frac{k_1}{k_2}\left(1 + \frac{k_3}{k_4}\right) \quad (mL/mL) \qquad (Eq.\ 1)$$

[^{18}F]FDG

Compartmental modeling of [^{18}F]FDG kinetics was performed as previously described (21–23). Briefly, a model of three compartments with five rate constants was used that is similar to that described for [^{11}C]3-OMG but with an additional tissue compartment and rate constant to represent phosphorylation of [^{18}F]FDG. In this article, to avoid confusion with the rate constants used for [^{11}C]3-OMG, those pertaining to [^{18}F]FDG are designated with an asterisk (k_n^*). Thus, k_1^*(mL/mL/min) and $k_2^*(min^{-1})$ describe the delivery of [^{18}F]-FDG from the capillary to the muscle interstitial space and reserve process, respectively; $k_3^*(min^{-1})$ and $k_4^*(min^{-1})$ describe inward and outward transport of [^{18}F]FDG; and $k_5^*(min^{-1})$ describes the phosphorylation of [^{18}F]FDG. From the five rate constants, the fractional uptake of [^{18}F]FDG can be determined, as represented by the macroparameter K (mL/mL/min) shown in Eq. 2:

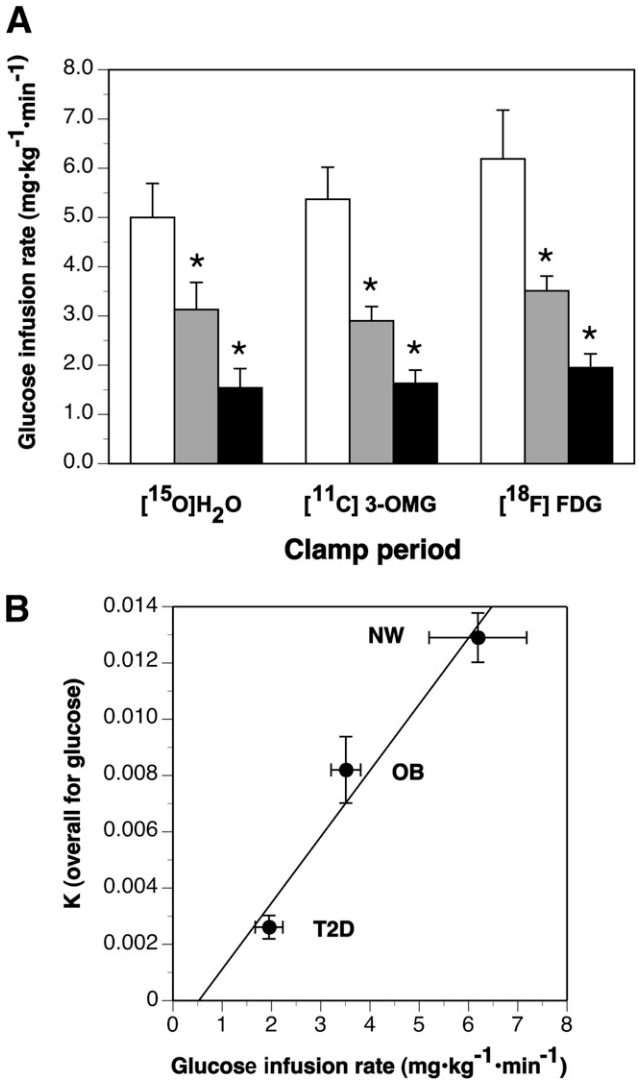

Figure 1—Glucose infusion rate and glucose infusion rate vs. K. *A*: Glucose infusion rate with each PET tracer. *A difference vs. NW, $P < 0.05$. White bars, NW; gray bars, OB; black bars, T2D. *B*: Glucose infusion rate vs. K (overall rate constant).

$$K = \frac{k_1^* k_3^* k_5^*}{k_2^* k_4^* + k_2^* k_5^* + k_3^* k_5^*} \quad (mL/mL/min) \qquad (Eq.\ 2)$$

Glucose

A specific glucose tracer was not used in this study; instead, a glucose model was developed from the kinetics determined using [^{11}C]3-OMG and [^{18}F]FDG, as previously described (12,21–25). Rate constants from compartmental modeling of [^{11}C]3-OMG were used for that of glucose, and a value for the rate constant of glucose phosphorylation (k_5) was additionally derived from the lumped constant (LC), as shown in Eq. 3:

$$k_5 = \frac{k_2 k_4 K}{k_1 k_3 LC - K \cdot (k_2 + k_3)} \quad (min^{-1}) \qquad (Eq.\ 3)$$

From glucose k_1–k_5 parameters, intracellular glucose concentration (Ce) was estimated, using Eq. 4 (16):

$$C_e = \frac{K_1 k_3}{k_2 k_4 + k_2 k_5 + k_3 k_5} C_p \text{ (plasma glucose)} \quad (mg/dL \text{ tissue}) \qquad (Eq.\ 4)$$

Following the theory of metabolic control analysis, the control coefficients (CC) of delivery, transmembrane transport, and phosphorylation were calculated as shown in Eq. 5 (17,26,27):

$$CC_{delivery} = \frac{k_3 k_5}{k_3 k_5 + k_2 k_5 + k_2 k_4}$$
$$CC_{transport} = \frac{k_2 k_5}{k_3 k_5 + k_2 k_5 + k_2 k_4} \qquad (Eq.\ 5)$$
$$CC_{phosphor} = \frac{k_2 k_4}{k_3 k_5 + k_2 k_5 + k_2 k_4}$$

The higher the value of a control coefficient, the more that this process is rate limiting and according a locus of control.

Statistics

Data are presented as mean ± SEM. One-way ANOVA was used to examine for significance of differences among subject groups. One-way repeated-measures ANOVA was used to compare basal and insulin group parameters. A $P < 0.05$ was considered significant.

RESULTS

Systemic and Muscle Insulin Sensitivity

The clinical characteristics of the research subjects are presented in Table 1, and the rates of exogenous glucose infusion during insulin infusion clamp studies are shown in Fig. 1*A*. Compared with NW, both OB and T2D manifested systemic IR, which was most severe in T2D ($P < 0.001$). Fasting glucose values were significantly different among T2D (144.0 ± 13.0 mg/dL), NW (96.5 ± 1.8 mg/dL), and OB (94.4 ± 1.5 mg/dL) ($P < 0.05$). Insulin levels were not significantly different among the three groups at fasting (NW 9.81 ± 0.94, OB 18.01 ± 3.54, T2D 18.39 ± 1.80 μU/mL) or insulin stimulation (NW 87.95 ± 2.18, OB 102.30 ± 8.89, T2D 102.52 ± 6.02 μU/mL). Free fatty acids were also not significantly different between the groups at fasting (NW 592 ± 65, OB 577 ± 30, T2D 532 ± 63 μmol/L) or insulin stimulation (NW 106 ± 33, OB 127 ± 31, T2D 167 ± 35 μU/mL). Skeletal muscle (soleus) insulin sensitivity, as measured by K, the macroscopic PET imaging parameter for [^{18}F]FDG uptake, was strongly correlated with respective glucose infusion rates as shown in Fig. 1*B*.

Tissue Perfusion ([^{15}O]H_2O)

Tissue perfusion in soleus muscle was lower ($P < 0.01$) in OB (0.0194 ± 0.0055 mL/min-mL) and T2D

(0.0125 ± 0.0022 mL/min-mL) than in NW (0.0316 ± 0.0139 mL/min-mL) during basal conditions. During insulin infusion, muscle tissue perfusion did not change significantly from basal conditions in any group. The k_1 parameter obtained from [^{11}C]3-OMG modeling, which describes tracer delivery from plasma to tissue, has values that are concordant with those obtained using [^{15}O]H_2O, a tracer that is used to measure solely tissue perfusion kinetics. This concordance of k_1 values for these two tracers is consistent with earlier findings (12,20,28).

Tissue Uptake of [^{11}C]3-OMG

The mean group soleus muscle tissue time–activity curves for [^{11}C]3-OMG are shown in Fig. 2*A* and *B* for basal and insulin-stimulated conditions, respectively. Using these data in conjunction with arterial plasma time–activity data, tissue data were modeled to estimate parameters describing both delivery (plasma to extracellular space) and bidirectional glucose transport for [^{11}C]3-OMG, and these parameters of the tracer kinetics that underlie the shapes of the tissue–activity curves are shown in Table 2. The kinetic parameter of great interest for this investigation of muscle IR is k_3, which described the inward transport for [^{11}C]3-OMG, a nonmetabolized glucose analog that has nearly identical affinity as glucose for glucose transporters (25). Across groups, the basal values for k_3 were similar (Fig. 3). During insulin infusion, k_3 increased sevenfold in NW participants, which is similar to earlier findings in lean nondiabetic subjects (12,19). In the OB subjects, the group mean value for k_3 increased sixfold over the basal condition, which is a similar response to that found in NW. However, in T2D, the group mean value for k_3 during insulin-stimulated conditions was significantly lower than in NW or OB ($P < 0.01$), and although the value increased during the insulin condition compared with the basal condition, the change was a twofold increase, which was a blunted response to insulin compared with the changes observed in the NW and OB nondiabetic groups. Because the transport of [^{11}C]3-OMG is bidirectional, the higher tissue activities and k_3 values in the NW and OB groups were associated with higher k_4 values (and greater changes in k_4 during insulin compared with basal conditions). As well, the higher efficiency of inward glucose transport during insulin-stimulated conditions was associated with reduced values for k_2, the parameter describing efflux from tissue (extracellular space) to plasma. In T2D, the insulin-stimulated versus basal changes in k_2 and k_4 were blunted compared with NW and OB. The insulin-resistant response of glucose transport in T2D is also evident within the volume of distribution parameters for [^{11}C]3-OMG (Table 2), which reveals that although there was evidence of soleus response to insulin in T2D compared with basal conditions, the amplitude of this response was attenuated in T2D, indicating that impaired insulin stimulation of glucose transport contributes strongly to muscle IR.

Tissue Uptake of [^{18}F]FDG

The key difference between [^{11}C]3-OMG and [^{18}F]FDG is that the latter glucose analog can be a substrate for hexokinase and undergo phosphorylation, which over the short time course of these PET imaging studies causes [^{18}F]FDG-6-P to be formed and irreversibly trapped within soleus muscle. The soleus muscle time–tissue activity curves for [^{18}F]FDG during basal and insulin-stimulated conditions are shown in Fig. 4*A* and *B*. During basal conditions, there was close similarities across groups, but during insulin-stimulated conditions, marked group differences became evident with sharply diminished tissue activity in T2D and a discernibly altered shape. For the goals of this investigation, to study the potential contribution of glucose phosphorylation to IR, the arterial and tissue activity for [^{18}F]FDG were used to determine K, the macroscopic parameter of irreversible tracer uptake. As described in the RESEARCH DESIGN AND METHODS, K was used in conjunction with kinetic parameters for [^{11}C]3-OMG and with the lumped constant to estimate the kinetics of actual glucose delivery, bidirectional transport, and phosphorylation. The kinetic parameters for [^{18}F]FDG are presented in Supplementary Table 1. These data will not be further discussed here other than to note that the findings across groups and between basal and insulin studies are similar to those for [^{11}C]3-OMG, with differences reflecting known analog effects for [^{18}F]FDG (as reflected in the lumped constant) and with the addition of k_5, the kinetic parameter ascribed to the formation of [^{18}F]FDG-6-P (Fig. 5).

The partition coefficient V_{ec} for glucose in the tissue extracellular compartment relative to plasma did not change from the basal to the insulin conditions. The partition coefficient V_{ic} for glucose in the tissue intracellular compartment relative to plasma increased during the insulin condition ($P < 0.05$) in NW and OB but not in T2D. $V_{ic}$was then used to calculate the intracellular glucose values when multiplied by the plasma glucose levels. Intracellular glucose levels were not significantly different at basal conditions, but under insulin stimulation, NW had significantly higher intracellular glucose levels than T2D (NW 33.7 ± 4.8, OB 31.3 ± 12.5, T2D 10.1 ± 2.0 mg/dL; $P < 0.05$).

Control Coefficient for Glucose Skeletal Muscle Uptake

The rate constants describing glucose kinetics were used to calculate the control coefficient for delivery ($CC_{delivery}$), transport ($CC_{transport}$), and phosphorylation ($CC_{phosphor}$) during the basal and insulin conditions are presented in Fig. 6. Glucose transport and phosphorylation (hexokinase) largely account for control of glucose kinetics in skeletal muscle during basal conditions. Of these, transport exerted stronger control than phosphorylation. Thus, glucose delivery was not found to substantially control glucose uptake into skeletal muscle during basal conditions. This pattern was consistent across all groups. For NW subjects, this pattern of distribution of control

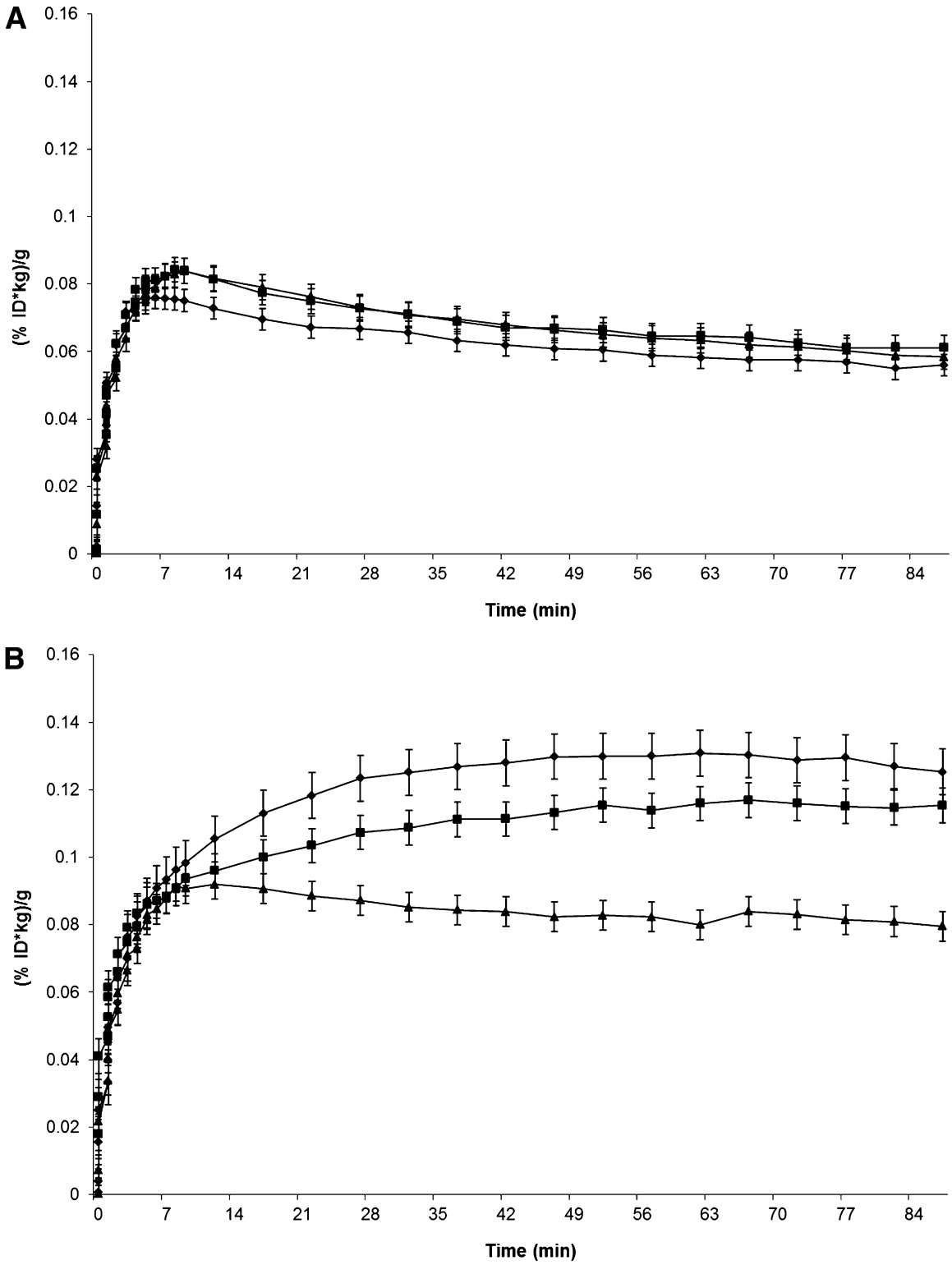

Figure 2—[^{11}C]3-OMG tissue–activity curves for the basal (*A*) and insulin-stimulated (*B*) conditions. ◆, NW; ■, OB; ▲, T2D. % ID*kg, percent of the injected dose of tracer * body weight in kg.

shifted during insulin conditions such that glucose delivery and transport contributed nearly equally to the control of glucose uptake and together accounted for 90% of control, whereas phosphorylation was calculated to manifest only the remaining 10% of rate control for the kinetics of glucose uptake. This was in contrast to that observed for T2D in which insulin-stimulated glucose uptake was predominantly, but not exclusively

Table 2—Kinetic parameters for [^{11}C]3-OMG

	Basal			Insulin Stimulation		
	NW	OB	T2D	NW	OB	T2D
k_1 (mL/mL/min)	0.024 ± 0.002 (3 ± 0.39)	0.023 ± 0.004 (3 ± 0.27)	0.019 ± 0.001 (3 ± 0.32)	0.021 ± 0.001 (3 ± 0.68)	0.019 ± 0.010 (6 ± 0.84)	0.018 ± 0.002 (4 ± 0.24)
k_2 (min^{-1})	0.185 ± 0.014 (6 ± 0.62)	0.178 ± 0.031 (6 ± 0.90)	0.141 ± 0.012 (5 ± 0.60)	0.110 ± 0.020 (16 ± 2.79)	0.152 ± 0.098 (15 ± 1.66)	0.130 ± 0.017 (7 ± 0.86)
k_3 (min^{-1})	0.015 ± 0.001 (19 ± 2.13)	0.012 ± 0.001 (17 ± 5.11)	0.011 ± 0.002 (14 ± 1.84)	0.104 ± 0.013 (22 ± 5.10)	0.080 ± 0.012 (15 ± 2.82)	0.023 ± 0.005* (13 ± 1.42)
k_4 (min^{-1})	0.027 ± 0.003 (17 ± 1.79)	0.023 ± 0.002 (21 ± 4.82)	0.019 ± 0.002 (22 ± 4.91)	0.056 ± 0.014 (7 ± 1.22)	0.026 ± 0.005 (9 ± 0.91)	0.014 ± 0.003† (23 ± 6.18)
V_{tt} (mL/mL)	0.205 ± 0.007 (3 ± 0.67)	0.205 ± 0.013 (4 ± 0.91)	0.217 ± 0.018 (5 ± 1.79)	0.702 ± 0.052 (7 ± 2.08)	0.555 ± 0.052 (3 ± 0.35)	0.392 ± 0.046† (10 ± 3.28)
V_{ec} (mL/mL)	0.132 ± 0.005 (3 ± 0.41)	0.132 ± 0.008 (3 ± 0.72)	0.139 ± 0.010 (3 ± 0.38)	0.234 ± 0.043 (13 ± 2.54)	0.136 ± 0.016 (10 ± 2.12)	0.144 ± 0.008 (4 ± 0.68)
V_{ic} (mL/mL)	0.073 ± 0.008 (6 ± 0.80)	0.073 ± 0.007 (10 ± 2.52)	0.078 ± 0.011 (13 ± 3.66)	0.467 ± 0.038 (8 ± 2.26)	0.418 ± 0.044 (5 ± 0.61)	0.248 ± 0.042* (15 ± 4.81)

Data are mean ± SEM (Values in parentheses are the errors for parameter estimation). V_{tt}, total volume of distribution for glucose (sum of V_{ec} and V_{ic}). *$P < 0.05$ vs. NW and OB. †$P < 0.05$ vs. NW.

controlled, that is, limited by glucose transport. Thus, the distribution of insulin-mediated glucose uptake was vastly different in T2D muscle.

DISCUSSION

To our knowledge, this study is the first to use three tracers ([^{15}O]H_2O, [^{11}C]3-OMG, and [^{18}F]FDG) during dynamic PET imaging to ascertain separate and specific defects in glucose metabolism in obesity and T2D. The primary findings were that lower insulin-stimulated glucose transport accounts for a quantifiable and substantial degree of IR in skeletal muscle of T2D and that additional defects in glucose phosphorylation characterize the IR of T2D.

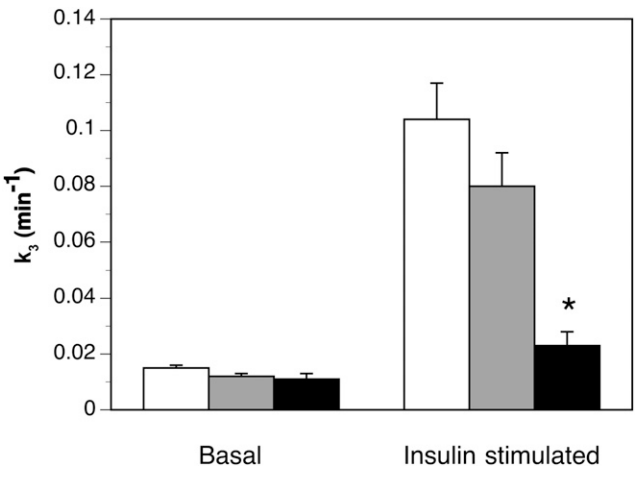

Figure 3—Inward glucose transport (k_3) at basal and insulin-stimulated conditions. White bars, NW; gray bars, OB; black bars, T2D. *A difference at $P < 0.05$ between T2D and both NW and OB.

Following an overnight fast, neither glucose transport nor phosphorylation was different in the skeletal muscle of OB or T2D compared with lean, healthy muscle. The predominant control of glucose uptake in the fasting state was at the level of glucose transport across all study groups, with some additional control posited by glucose phosphorylation. Glucose delivery exerted only negligible control, although this was quantitatively lower in muscle in T2D. The lower basal muscle blood flow in diabetes could perhaps reflect a lower capillary density or perfusion (29). These observations are consistent with other studies showing that basal glucose uptake is not impaired in IR and diabetes (30) and that glucose transport is the rate-limiting step in basal glucose uptake (30).

The glucose infusion rates in response to physiological levels of insulin were lower for OB subjects, and this systemic IR was more severe in T2D, which was strongly associated with the macroscopic index of muscle glucose flux assessed by PET. The lower rates of glucose transport and fractional phosphorylation in OB than in NW, although not as markedly low as in T2D, clearly indicate that skeletal muscle IR in OB, along with normal fasting glycemia, helps to define the prediabetic state. This is consistent with values reported in earlier studies in normal weight subjects using similar protocols (12,19). However, despite the nearly 50% lower systemic glucose infusion rates in OB subjects, their lower insulin-stimulated increase in glucose transport was not statistically different, suggesting that obesity alone has less dramatic effects of inward glucose transport despite fairly marked systemic IR. The small number of subjects could have limited our ability to quantify the obesity-related defects in glucose transport, particularly given the heterogeneity of insulin sensitivity in obesity. Moreover, the systemic

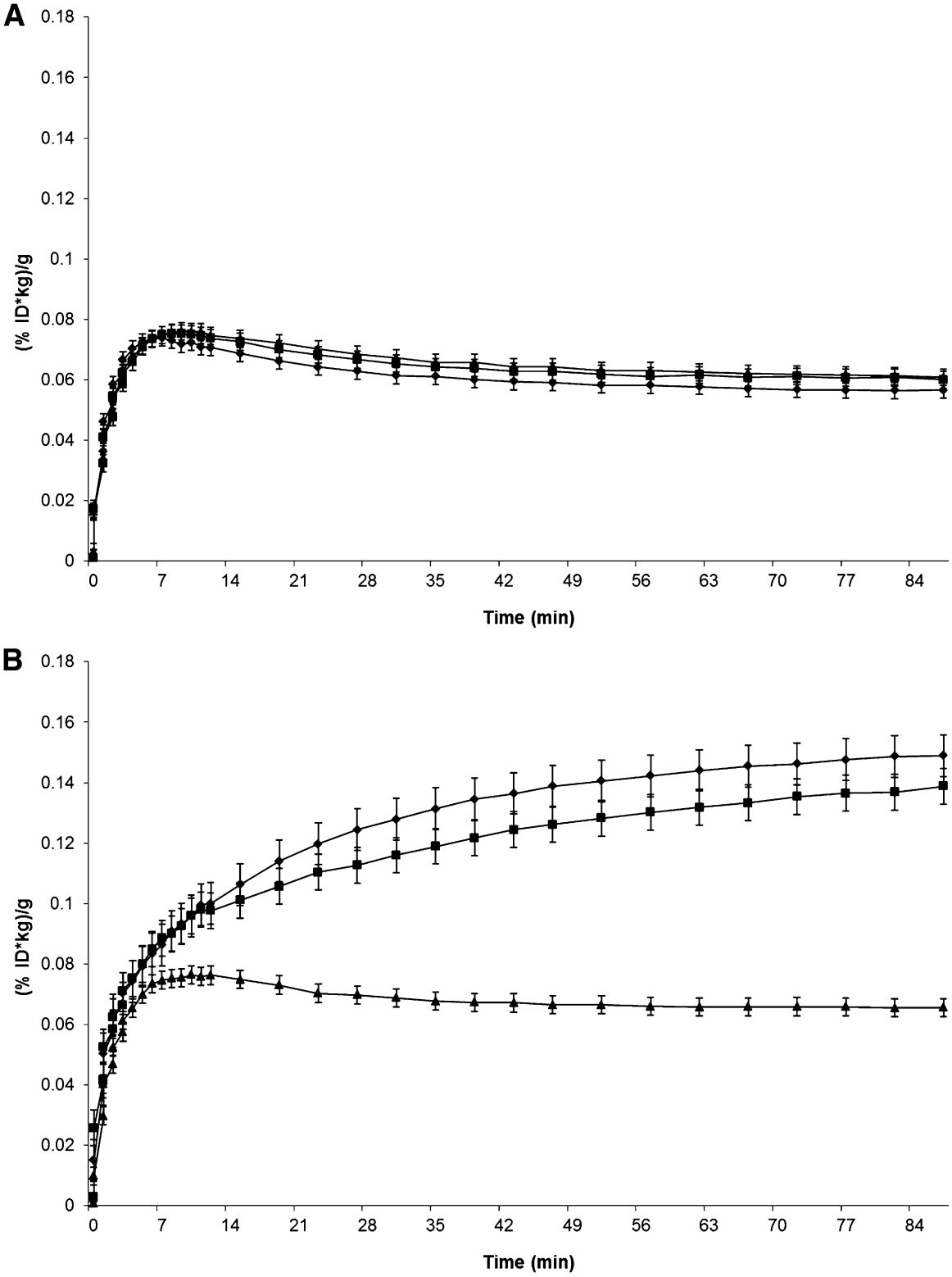

Figure 4—[^{18}F]FDG tissue–activity curves for the basal (*A*) and insulin-stimulated (*B*) conditions. ◆, NW; ■, OB; ▲, T2D. % ID*kg, percent of the injected dose of tracer * body weight in kg.

insulin sensitivity could have been confounded by hepatic IR, which again, highlights the utility of PET to quantify skeletal muscle glucose metabolism. We also note that a lean, T2D group was not included, which could have further quantified the effects of both obesity and T2D. Additionally, we recognize that even though our sex ratios were similar, there could be sex-specific differences in metabolic disease that may have influenced

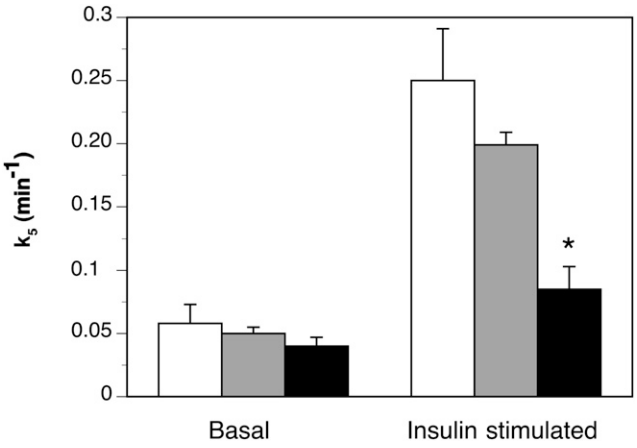

Figure 5—Fractional phosphorylation of glucose (k_5) under basal and insulin-stimulated conditions. White bars, NW; gray bars, OB; black bars, T2D. *A difference at $P < 0.05$ between T2D and both NW and OB.

the findings. In stark contrast, skeletal muscle in T2D had much lower fractional glucose transport rates and intracellular glucose levels. These results are consistent with lower muscle GLUT4 content and translocation in T2D (30–33) and with the slight accumulation of free glucose in response to insulin (4,8,10), all of which have been interpreted as defects in glucose transport and comprising a major limitation to glucose uptake in response to insulin. Although bidirectional glucose transport within muscle can be assessed directly in vitro, the in vivo glucose transport also depends on delivery to the tissue. The time–tissue activity curves for 3-OMG reflect an integration of these two reversible processes (12,20,28), which the current study distinguished using sequential imaging with [^{15}O]H_2O and [^{11}C]3-OMG. Insulin-stimulated rates of muscle tissue perfusion were similar across subject groups and are similar to those reported previously for normal weight subjects (34). These rates corresponded very well with kinetic values for tissue perfusion attributed to k_1 ascertained for [^{11}C]3-OMG and [^{18}F]FDG. Rates of tissue perfusion did not change significantly in response to insulin compared with fasting. This does not discount the hemodynamic effects of insulin to stimulate capillary recruitment, as has been demonstrated (35,36), which is beyond the spatial resolution of PET. Improving spatial resolution with PET may provide additional insight into the dynamic interaction between glucose delivery and transport in IR. NW subjects in the current study had a redistribution of control of glucose uptake from predominantly glucose transport

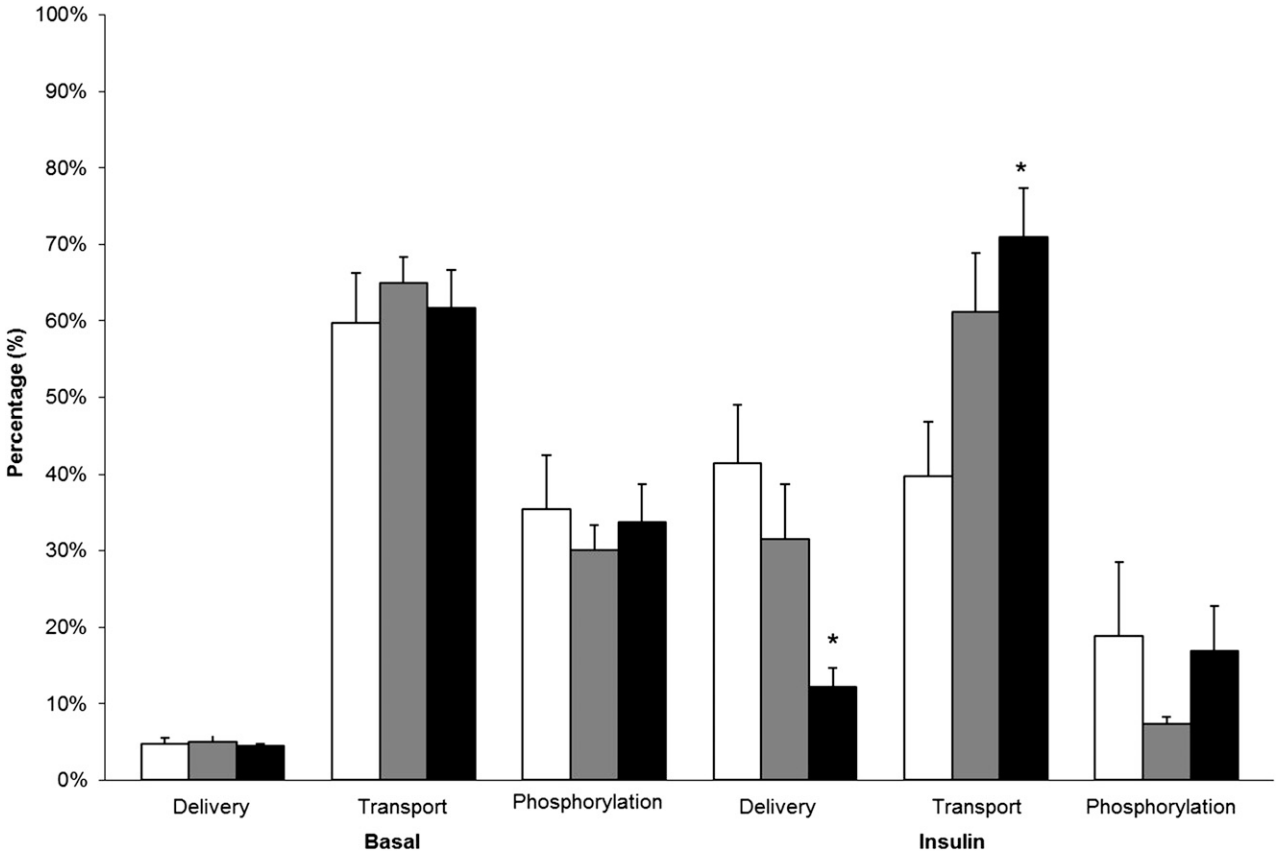

Figure 6—Control coefficients for delivery, transport, and phosphorylation. Control coefficients representing the distribution of control among the proximal steps of skeletal muscle (soleus) glucose metabolism under basal and insulin-stimulated conditions. White bars, NW; gray bars, OB; black bars, T2D. *$P < 0.05$ T2D vs. NW.

in the fasting state to greater control by delivery in response to insulin, which was not observed for muscle in OB or T2D subjects. Thus, the greater control of glucose uptake by insulin in muscle of NW subjects is consistent with in vivo studies in rodents, indicating that insulin-stimulated glucose uptake is constrained by delivery (11,14,37). This is also in accord with a major defect in insulin-stimulated glucose transport in diabetic muscle in the current study.

The insulin-stimulated fractional phosphorylation of glucose was significantly lower in muscle in diabetes. Thus, after accounting for glucose delivery and lower glucose transport in diabetes ascertained specifically with [^{11}C]3-OMG, an additional defect in glucose phosphorylation exists in insulin-resistant diabetic muscle. This defect was quite pronounced in diabetic muscle and was not as obvious in muscle of OB subjects. This finding could reflect the heterogeneity or wider range in the severity of IR of obesity and suggests that obesity per se does not unequivocally cause defects in skeletal muscle glucose metabolism but, nevertheless, contributes to the underlying progression of IR eventually causing T2D. Dynamic PET imaging performed using [^{18}F]FDG indicated that glucose phosphorylation does not exert strong rate control on glucose uptake during insulin-stimulated conditions in muscle of NW subjects but still distinguishes skeletal muscle IR in T2D. This is similar to a previous article that used dynamic PET studies modeling [^{18}F]FDG uptake kinetics to observe a major defect in glucose transmembrane transport with an additional, albeit smaller, defect in glucose phosphorylation (23). The current study extends these findings in two very important ways. First, the use of multiple PET tracers in the same subject has allowed us to separate and quantify the proximal steps of glucose transport and phosphorylation with considerably less dependence on mathematical modeling of kinetic data. Second, we have now more clearly shown for the first time using these multiple PET tracers that glucose phosphorylation is impaired in skeletal muscle in T2D after accounting for defects in glucose transport. This is consistent with reports in animal models demonstrating additional defects in insulin-stimulated glucose phosphorylation (1,11,13,14,38–40). Both GLUT4 and hexokinase are coordinately regulated (41), and both track strongly with oxidative capacity and capillary density in muscle, all of which have been consistently demonstrated to be affected in T2D (30,31,33,42).

In summary, dynamic PET imaging of skeletal muscle glucose metabolism reveals a major defect in glucose transport, which defines much of the severity of IR of T2D, and that an additional impairment within the efficiency of glucose phosphorylation is present. In contrast to lean, healthy skeletal muscle in which the control of insulin-stimulated glucose uptake is more broadly distributed across each of the proximal steps of glucose delivery, transport, and phosphorylation, the rate-limiting control of glucose metabolism in muscle in T2D is posited mostly at glucose transport, with smaller control being manifest at glucose delivery and phosphorylation. These triple-tracer PET imaging data have important implications for clinical treatment of T2D, and these methodologies could be valuable in determining whether these defects persist at higher doses of insulin and which specific control points may be rectified with insulin-sensitizing interventions.

Acknowledgments. The authors acknowledge the efforts and cooperation of the research volunteers and the support from the staffs of the University of Pittsburgh General Clinical Research Center and the PET Center.

Funding. These studies were supported by the National Institutes of Health, National Institute of Diabetes and Digestive and Kidney Diseases (NIH-NIDDK) (DK-60555-02), by the University of Pittsburgh General Clinical Research Center (5M01-RR-00056), and by the Obesity and Nutrition Research Center (NIH-NIDDK, P30-DK-46204). This work was also supported by NIH grant EB-01975.

Duality of Interest. R.R.P. is currently employed by Amylin Pharmaceuticals. D.E.K. is currently employed by Merck Sharp & Dohme Corp. No other potential conflicts of interest relevant to this article were reported.

Author Contributions. B.H.G. supervised the project and wrote the manuscript. A.B. performed the modeling analysis. J.M.N. researched the data, contributed to the discussion, and reviewed and edited the manuscript. K.A., R.R.P., and C.K. researched the data. J.C.P. and C.C. contributed to the modeling analysis. D.E.K. contributed to the discussion and reviewed and edited the manuscript. B.H.G. is the guarantor of this work and, as such, had full access to all the data in the study and takes responsibility for the integrity of the data and the accuracy of the data analysis.

References

1. Furler SM, Jenkins AB, Storlien LH, Kraegen EW. In vivo location of the rate-limiting step of hexose uptake in muscle and brain tissue of rats. Am J Physiol 1991;261:E337–E347
2. Bonadonna RC, Saccomani MP, Seely L, et al. Glucose transport in human skeletal muscle. The in vivo response to insulin. Diabetes 1993;42:191–198
3. Post RL, Morgan HE, Park CR. Regulation of glucose uptake in muscle. III. The interaction of membrane transport and phosphorylation in the control of glucose uptake. J Biol Chem 1961;236:269–272
4. Cline GW, Petersen KF, Krssak M, et al. Impaired glucose transport as a cause of decreased insulin-stimulated muscle glycogen synthesis in type 2 diabetes. N Engl J Med 1999;341:240–246
5. Shepherd PR, Kahn BB. Glucose transporters and insulin action—implications for insulin resistance and diabetes mellitus. N Engl J Med 1999;341:248–257
6. Lund S, Holman GD, Schmitz O, Pedersen O. Glut 4 content in the plasma membrane of rat skeletal muscle: comparative studies of the subcellular fractionation method and the exofacial photolabelling technique using ATB-BMPA. FEBS Lett 1993;330:312–318
7. Ramlal T, Sarabia V, Bilan PJ, Klip A. Insulin-mediated translocation of glucose transporters from intracellular membranes to plasma membranes: sole mechanism of stimulation of glucose transport in L6 muscle cells. Biochem Biophys Res Commun 1988;157:1329–1335
8. Cline GW, Jucker BM, Trajanoski Z, Rennings AJ, Shulman GI. A novel ^{13}C NMR method to assess intracellular glucose concentration in muscle, in vivo. Am J Physiol 1998;274:E381–E389

9. Kahn BB. Lilly lecture 1995. Glucose transport: pivotal step in insulin action. Diabetes 1996;45:1644–1654
10. Katz A, Nyomba BL, Bogardus C. No accumulation of glucose in human skeletal muscle during euglycemic hyperinsulinemia. Am J Physiol 1988; 255:E942–E945
11. Halseth AE, Bracy DP, Wasserman DH. Limitations to exercise- and maximal insulin-stimulated muscle glucose uptake. J Appl Physiol (1985) 1998;85:2305–2313
12. Bertoldo A, Pencek RR, Azuma K, et al. Interactions between delivery, transport, and phosphorylation of glucose in governing uptake into human skeletal muscle. Diabetes 2006;55:3028–3037
13. Fueger PT, Hess HS, Posey KA, et al. Control of exercise-stimulated muscle glucose uptake by GLUT4 is dependent on glucose phosphorylation capacity in the conscious mouse. J Biol Chem 2004;279:50956–50961
14. Fueger PT, Hess HS, Bracy DP, et al. Regulation of insulin-stimulated muscle glucose uptake in the conscious mouse: role of glucose transport is dependent on glucose phosphorylation capacity. Endocrinology 2004;145: 4912–4916
15. Watson CC, Newport D, Casey ME, DeKemp RA, Beanlands RS, Schmand M. Evaluation of simulation-based scatter correction for 3-D PET cardiac imaging. IEEE Trans Nucl Sci 1997;44:90–97
16. Woods RP, Mazziotta JC, Cherry SR. MRI-PET registration with automated algorithm. J Comput Assist Tomogr 1993;17:536–546
17. Minoshima S, Berger KL, Lee KS, Mintun MA. An automated method for rotational correction and centering of three-dimensional functional brain images. J Nucl Med 1992;33:1579–1585
18. Kety SS. The theory and applications of the exchange of inert gas at the lungs and tissues. Pharmacol Rev 1951;3:1–41
19. Pencek RR, Bertoldo A, Price J, Kelley C, Cobelli C, Kelley DE. Dose-responsive insulin regulation of glucose transport in human skeletal muscle. Am J Physiol Endocrinol Metab 2006;290:E1124–E1130
20. Bertoldo A, Price J, Mathis C, et al. Quantitative assessment of glucose transport in human skeletal muscle: dynamic positron emission tomography imaging of [O-methyl-^{11}C]3-O-methyl-D-glucose. J Clin Endocrinol Metab 2005;90:1752–1759
21. Bertoldo A, Peltoniemi P, Oikonen V, Knuuti J, Nuutila P, Cobelli C. Kinetic modeling of [(18)F]FDG in skeletal muscle by PET: a four-compartment five-rate-constant model. Am J Physiol Endocrinol Metab 2001;281:E524–E536
22. Bertoldo A, Vicini P, Sambuceti G, Lammertsma AA, Parodi O, Cobelli C. Evaluation of compartmental and spectral analysis models of [^{18}F]FDG kinetics for heart and brain studies with PET. IEEE Trans Biomed Eng 1998; 45:1429–1448
23. Williams KV, Bertoldo A, Mattioni B, Price JC, Cobelli C, Kelley DE. Glucose transport and phosphorylation in skeletal muscle in obesity: insight from a muscle-specific positron emission tomography model. J Clin Endocrinol Metab 2003;88:1271–1279
24. Carruthers A. Facilitated diffusion of glucose. Physiol Rev 1990;70:1135–1176
25. Bonadonna RC, Saccomani MP, Cobelli C. In vivo glucose transport in human skeletal muscle: tools, problems and perspectives. Baillieres Clin Endocrinol Metab 1993;7:929–960
26. Heinrich R, Rapoport TA. A linear steady-state treatment of enzymatic chains. General properties, control and effector strength. Eur J Biochem 1974;42:89–95
27. Kacser H, Burns JA. The control of flux. Symp Soc Exp Biol 1973;27:65–104
28. Huang S, Phelps M. Principles of tracer kinetic modeling in positron emission tomography and autoradiography. In *Positron Emission Tomography and Autoradiography: Principles and Applications for the Brain and Heart*. Phelps M, Mazziotta J, Schelbert H, Eds. New York, Raven Press, 1986, p. 287–346
29. Baron AD. Hemodynamic actions of insulin. Am J Physiol 1994;267:E187–E202
30. Kelley DE, Mintun MA, Watkins SC, et al. The effect of non-insulin-dependent diabetes mellitus and obesity on glucose transport and phosphorylation in skeletal muscle. J Clin Invest 1996;97:2705–2713
31. Garvey WT, Maianu L, Zhu JH, Brechtel-Hook G, Wallace P, Baron AD. Evidence for defects in the trafficking and translocation of GLUT4 glucose transporters in skeletal muscle as a cause of human insulin resistance. J Clin Invest 1998;101:2377–2386
32. Ryder JW, Yang J, Galuska D, et al. Use of a novel impermeable biotinylated photolabeling reagent to assess insulin- and hypoxia-stimulated cell surface GLUT4 content in skeletal muscle from type 2 diabetic patients. Diabetes 2000;49:647–654
33. Zierath JR, He L, Gumà A, Odegoard Wahlström E, Klip A, Wallberg-Henriksson H. Insulin action on glucose transport and plasma membrane GLUT4 content in skeletal muscle from patients with NIDDM. Diabetologia 1996;39:1180–1189
34. Raitakari M, Nuutila P, Ruotsalainen U, et al. Evidence for dissociation of insulin stimulation of blood flow and glucose uptake in human skeletal muscle: studies using [^{15}O]H2O, [^{18}F]fluoro-2-deoxy-D-glucose, and positron emission tomography. Diabetes 1996;45:1471–1477
35. Clark MG, Wallis MG, Barrett EJ, et al. Blood flow and muscle metabolism: a focus on insulin action. Am J Physiol Endocrinol Metab 2003;284:E241–E258
36. Rattigan S, Clark MG, Barrett EJ. Hemodynamic actions of insulin in rat skeletal muscle: evidence for capillary recruitment. Diabetes 1997;46:1381–1388
37. Halseth AE, Bracy DP, Wasserman DH. Functional limitations to glucose uptake in muscles comprised of different fiber types. Am J Physiol Endocrinol Metab 2001;280:E994–E999
38. Fueger PT, Shearer J, Bracy DP, et al. Control of muscle glucose uptake: test of the rate-limiting step paradigm in conscious, unrestrained mice. J Physiol 2005;562:925–935
39. Halseth AE, Bracy DP, Wasserman DH. Limitations to basal and insulin-stimulated skeletal muscle glucose uptake in the high-fat-fed rat. Am J Physiol Endocrinol Metab 2000;279:E1064–E1071
40. Halseth AE, Bracy DP, Wasserman DH. Overexpression of hexokinase II increases insulin and exercise-stimulated muscle glucose uptake in vivo. Am J Physiol 1999;276:E70–E77
41. Kong X, Manchester J, Salmons S, Lawrence JC Jr. Glucose transporters in single skeletal muscle fibers. Relationship to hexokinase and regulation by contractile activity. J Biol Chem 1994;269:12963–12967
42. Kelley DE, He J, Menshikova EV, Ritov VB. Dysfunction of mitochondria in human skeletal muscle in type 2 diabetes. Diabetes 2002;51:2944–2950